

PAPER

Dense fibroadhesive scarring and poor blood vessel-maturation hamper the integration of implanted collagen scaffolds in an experimental model of spinal cord injury

To cite this article: Haktan Altinova *et al* 2020 *Biomed. Mater.* **15** 015012

View the [article online](#) for updates and enhancements.



IOP | ebooks™

Bringing you innovative digital publishing with leading voices to create your essential collection of books in STEM research.

Start exploring the collection - download the first chapter of every title for free.

Biomedical Materials



PAPER

Dense fibroadhesive scarring and poor blood vessel-maturation hamper the integration of implanted collagen scaffolds in an experimental model of spinal cord injury

RECEIVED
18 September 2019

REVISED
1 December 2019

ACCEPTED FOR PUBLICATION
3 December 2019

PUBLISHED
13 February 2020

Haktan Altinova^{1,2,3,8} , Sebastian Hammes^{2,4,8}, Moniek Palm², Pascal Achenbach², Jose Gerardo-Nava^{3,5}, Ronald Deumens^{2,6}, Tobias Führmann⁷ , Sabien G A van Neerven⁶, Emmanuel Hermans⁶, Joachim Weis² and Gary A Brook²

¹ Department of Neurosurgery, RWTH Aachen University Hospital, Aachen, Germany

² Institute of Neuropathology, RWTH Aachen University Hospital, Aachen, Germany

³ Police Headquarters Berlin, Medical Commission, Berlin, Germany

⁴ Department of Surgery, RWTH Aachen University Hospital, Aachen, Germany

⁵ DWI-Leibniz Institute for Interactive Materials, Aachen, Germany

⁶ Institute of Neuroscience, Université Catholique de Louvain, Brussels, Belgium

⁷ Donnelly Centre for Cellular and Biomolecular Research, University of Toronto, Toronto, Canada

⁸ Joint first authorship; both authors contributed equally to this work.

E-mail: Haktan.Altinova@t-online.de

Keywords: spinal cord injury, type-I collagen scaffold, blood-spinal cord barrier, angiogenesis, CNS-scarring, fibrotic encapsulation

Supplementary material for this article is available [online](#)

Abstract

Severe spinal cord injury (SCI) results in permanent functional deficits, which despite pre-clinical advances, remain untreatable. Combinational approaches, including the implantation of bioengineered scaffolds are likely to promote significant tissue repair. However, this critically depends on the extent to which host tissue can integrate with the implant. In the present paper, blood vessel formation and maturation were studied within and around implanted micro-structured type-I collagen scaffolds at 10 weeks post implantation in adult rat mid-cervical spinal cord lateral funiculotomy injuries. Morphometric analysis revealed that blood vessel density within the scaffold was similar to that of the lateral white matter tracts that the implant replaced. However, immunohistochemistry for *zonula occludens*–1 (ZO-1) and endothelial barrier antigen revealed that scaffold microvessels remained largely immature, suggesting poor blood-spinal cord barrier (BSB) reformation. Furthermore, a band of intense ZO-1-immunoreactive fibroblast-like cells isolated the implant. Spinal cord vessels outside the ZO-1-band demonstrated BSB-formation, while vessels within the scaffold generally did not. The formation of a double-layered fibrotic and astroglial scar around the collagen scaffold might explain the relatively poor implant-host integration and suggests a mechanism for failed microvessel maturation. Targeted strategies that improve implant-host integration for such biomaterials will be vital for future tissue engineering and regenerative medicine approaches for traumatic SCI.

1. Introduction

The devastating, long-term motor, sensory and autonomic deficits following severe, traumatic spinal cord injury (SCI) are the result of acute damage to neurovascular tissues at the lesion site as well as the initiation of a cascade of secondary degenerative events that exaggerate tissue loss, promote fibroglial scarring and cystic cavitation [1–8].

Characterisation of the cellular and molecular events of secondary degeneration has resulted in the

development of a wide range of therapeutic strategies that, to some extent, improve functional outcome in experimental models of injury [9–12]. Such strategies are intended to shift the balance between axon-growth promoting and inhibitory conditions at the lesion site, for example by the delivery of pharmacological agents or other bioactive molecules such as neurotrophic factors, antibodies or enzymes, as well as the implantation of glial or progenitor cells [7, 13, 14]. It is widely acknowledged that future therapeutic strategies are likely to include combinations of these approaches to

induce tissue repair and functional recovery [9, 12]. A rapidly growing area of tissue engineering and regenerative medicine that may contribute to such combinational strategies is the development of implantable scaffolds intended to bridge the lesion site [10, 15]. A large number of natural and synthetic polymers have been used to generate such scaffolds, with specific nano- or micro-architectures which are also capable of delivering bioactive agents and growth-promoting cells [16–18]. Amongst the range of natural polymers being developed for traumatic SCI, scaffolds based on collagen have been reported to be promising candidates due to their biocompatibility, the natural abundance of collagen and the ability to manipulate it into a wide range of three-dimensional structures. Furthermore, the intrinsic cell-signaling motifs of collagen, and the ability to tailor its rate of biodegradation by cross-linking agents make this a highly versatile polymer [14, 19].

Our earlier *in vitro* studies have demonstrated the biocompatibility of a longitudinally micro-porous form of type-I collagen scaffold with neurons and glia from the central nervous system (CNS) and peripheral nervous system, as well as with non-neural cells such as fibroblasts [20–24]. Data revealed that astroglia were capable of substantial adhesion and migration into the micro-porous type-I collagen scaffolds [21] and that astrocytes as well as other populations of cells, such as Schwann cells and fibroblasts, could mix intimately within the scaffold in support of axon growth [22]. Such micro-porous collagen scaffolds have been used in an attempt to bridge complete or partial experimental lesions of the adult rat spinal cord [25–29]. Although some degree of functional recovery has been observed in the affected forepaw, this could not be correlated with a significant increase in axonal regeneration across the scaffold. Indeed, the implanted scaffold was poorly penetrated by host axons or astrocytes [30]. Attempts to improve implant-host integration and functional recovery by pre-seeding the collagen scaffold with syngeneic olfactory ensheathing cells only induced a trend for increased axonal growth into the scaffold, and reactive host astroglia largely failed to penetrate the scaffold [31]. As part of the development of such bioengineered scaffolds, it is important to understand the benefits as well as any possible shortcomings of the materials. Therefore, our recent efforts have focused on the host scarring response initiated by the implantation of the collagen scaffold into defined resection injuries of the adult rat spinal cord to obtain a better characterisation of the mechanism(s) involved in the prevention of scaffold-host integration. This has already revealed an encapsulating response by fibroblast-like cells that appeared to prevent the vast majority of neural profiles from entering the scaffold [32].

In the present investigation, the interactions of the implanted collagen scaffold with the host spinal cord have been further studied with particular emphasis on microvascular re-modelling and the disruption of the

blood-spinal cord barrier (BSB, [33]). The induction of angiogenesis has been correlated with enhanced tissue repair following traumatic CNS injury [34, 35], and newly formed blood vessels have been shown to act as substrates for guiding axon regeneration [34]. We therefore investigated new blood vessel formation and maturation in response to collagen scaffold implantation into defined model of SCI in the adult rat. We report that implantation induced an angiogenic response within the scaffold that lacked microvessel maturation, as indicated by a paucity of *zonula occludens*-1 (ZO-1) and endothelial barrier antigen (EBA) immunoreactivity. This suggests that the environment of such implants fails to promote successful BSB reformation. Furthermore, ZO-1-immunohistochemistry unexpectedly revealed the intense staining of overlapping layers of fibroblast-like cells that formed a band around the implant, partially encapsulating the scaffold. These observations strongly suggest that such type-I collagen scaffolds do not foster the reformation of a vascular bed within the implant that recapitulates the properties of CNS-microvessels, possibly due to the involvement of a novel and, as yet, poorly defined aspect of the host scarring response to the implant.

2. Material and methods

2.1. Experimental animals

All surgical procedures and animal handling were performed at the Institute of Neuroscience, Group of Neuropharmacology, Université Catholique de Louvain (UCLouvain), Belgium, according to the EU directive of 22nd September 2010 and granted by the local ethical committee on animal experimentation (2014/UCL/MD/012) and by the Belgian authority on animal experimentation (LA1230618). Adult female Sprague-Dawley rats ($n = 24$, body weight 180–200 g) were bred in the local UCLouvain animal facility and were housed in standard makrolon cages (2–3 animals per cage) under 12:12 h light-dark cycles. Food and water were provided *ad libitum*. All measures were taken to minimize the number of animals used, and to prevent pain and discomfort during the experiments.

2.2. Surgical procedure

The experimental spinal cord resection injuries were performed as described previously [32]. Briefly, a subcutaneous injection of buprenorphine ($0,1 \text{ mg kg}^{-1}$ body weight) was administered to all animals 30–60 min before surgery. Anaesthesia was induced by isoflurane inhalation delivered by a U-400 anaesthesia unit (Agntho's, Lidingö, Sweden, 4%–5% mixture in air for induction and maintained with a 2% mixture in air). Ophthalmic ointment was applied to prevent corneal drying. The shoulder and neck area were shaved and disinfected, followed by a mid-line skin incision and

blunt dissection of the neck musculature to expose the C3-C4 vertebrae and facilitate a right-sided hemilaminectomy. Using a dissection microscope and microscissors, a small dural window was opened followed by a right-sided, 2 mm wide lateral funiculotomy. Completeness of the resection injury was checked microscopically after aspiration and purging of the resection-gap. During surgery, care was taken to spare major spinal cord blood vessels to prevent severe bleeding and excessive local ischemia. Experimental animals were randomly allocated into two different groups: those receiving a lesion-only (i.e. control group, $n = 12$) and those receiving an orientated micro-structured type-I collagen scaffold (i.e. experimental group, $n = 12$) (Optimaix, Matricel GmbH, Herzogenrath, Germany). The collagen scaffold was trimmed and positioned into the resection-gap with its longitudinally orientated pores following the long axis of the spinal cord. After haemostasis, the dural flap was sutured using 10/0 sutures (Ethicon, Inc., Somerville, USA) and the layers of neck musculature and skin were realigned and sutured with 4/0 Prolene® (Ethicon Inc., Somerville, USA).

2.3. Tissue processing and histological analyses

At 10 weeks post-surgery (wps), animals were sacrificed in a euthanasia chamber by exposing them to high concentrations of carbon dioxide. After respiratory arrest, animals were transcardially perfused with 100 ml phosphate buffered saline (PBS, pH 7.4) followed by 300 ml of cold 4% paraformaldehyde in 0.1 M phosphate buffer. The fixed spinal cords were then dissected and post-fixed in the same fixative solution for 24 h, followed by cryoprotection in 30% sucrose in PBS. Tissue blocks of approximately 1 cm length ($n = 8$ lesion-only; $n = 8$ scaffold-implanted), centred around the lesion/implantation site, were then removed, frozen in powdered dry-ice and longitudinally cryosectioned (25 μm thick) using a Leica CM3040S cryostat. The remaining lesion/implantation tissue blocks ($n = 4$ lesion-only; $n = 4$ scaffold-implanted) were sectioned in a transverse plane (10 μm thick). Serial sections were mounted onto adjacent Superfrost Plus slides (R. Langenbrinck GmbH, Germany) such that the distance between adjacent longitudinal sections on each slide was 250 μm for longitudinal sections and 200 μm for adjacent transverse sections. All slides were then stored at -80°C until further immunohistochemical processing.

For immunofluorescence, the following primary antibodies were used: mouse anti-neurofilament 200 kDa (NF200, Clone NE 14, 1:2000, Sigma Aldrich MERCK, USA), mouse anti-rat-endothelial-cell-antigen-1 (RECA-1, 1:500, Bio-Rad, USA), mouse anti-endothelial-barrier-antigen (IgM) (EBA, clone SMI-71, 1:10 000, Biolegend, USA), mouse anti-vimentin (clone V9, 1:200, Sigma Aldrich MERCK, USA), mouse anti-gial-fibrillary-acidic-protein (GFAP, Clone GA5, 1:2000, MERCK), rabbit anti-zonula-occludens-

protein-1 (ZO-1, 1:500, Life Technologies, Germany) and rabbit anti-aquaporin-4 (Aqp-4, clone H80, 1:500, Santa Cruz Biotechnologies, USA). Prior to immunofluorescence, antigen retrieval was performed by heating samples to 37°C in citrate buffer (pH 6, Code S1699, DAKO, Germany) for 5 h. All solutions were prepared in antibody diluent, consisting of PBS containing 1% Triton X-100 (Sigma Aldrich, MERCK, USA) and 1% bovine serum albumin (Carl Roth, Germany), and all immunohistochemical steps took place at room temperature.

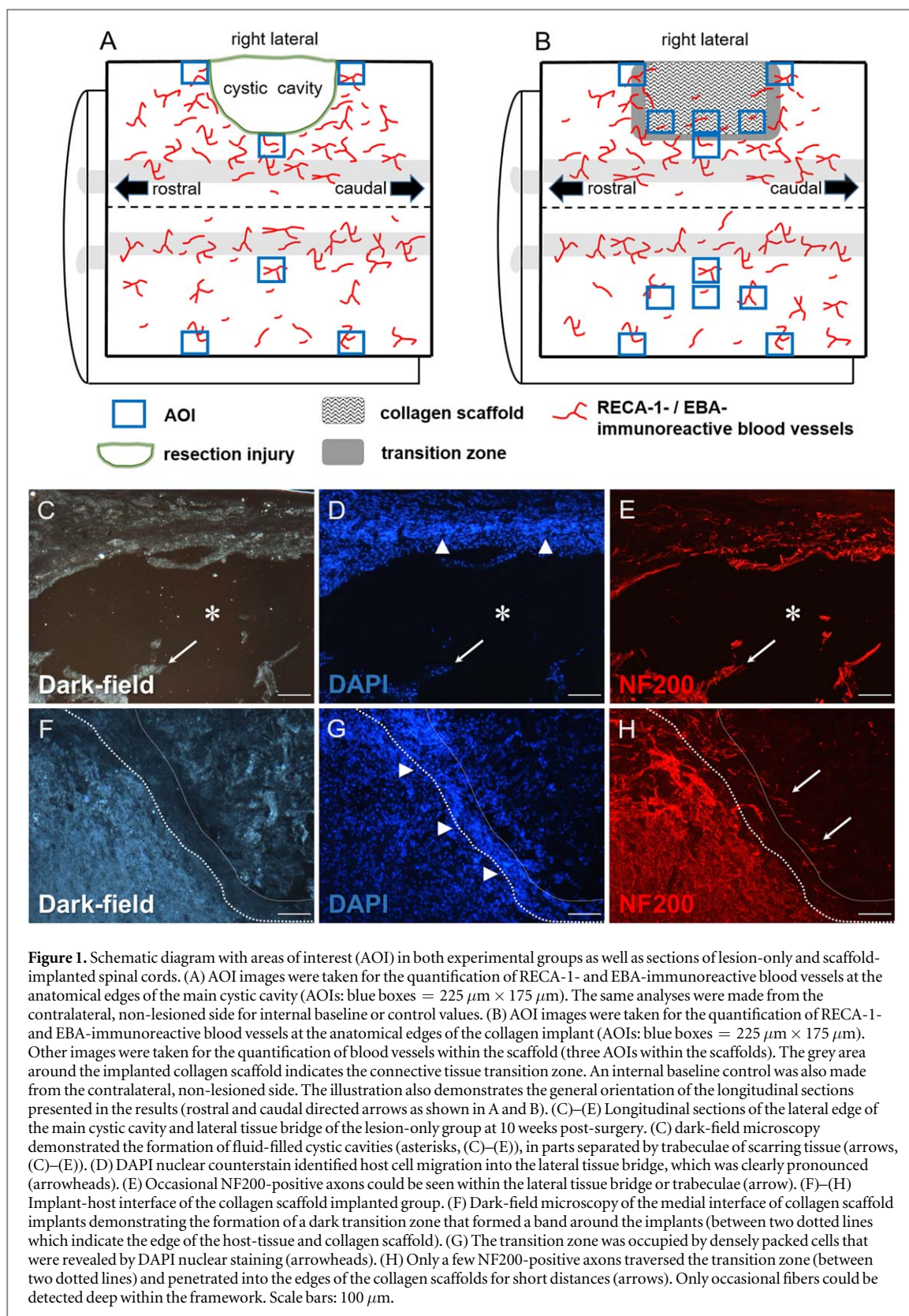
Sections were incubated in 10% normal goat serum (Jackson ImmunoResearch, UK) for 1 h after an initial washing step in PBS to block non-specific antibody interactions. The sections were then incubated overnight with combinations of primary antibodies. The next day, sections were washed in PBS and incubated with the fluorochrome-conjugated secondary antibodies (diluted at 1:500) for 2 h: Alexa-488 conjugated goat-anti-rabbit IgG, Alexa-594 conjugated goat-anti-mouse IgG or Alexa-594 conjugated goat-anti-mouse IgM (for EBA, Thermofisher Scientific, USA). A nuclear counterstain was performed by adding 1 $\mu\text{g}/\text{ml}$ of DNA-intercalator 4',6-diamino-2-phenylindole (DAPI, Sigma-Aldrich MERCK, USA) to the secondary antibody solutions and sections were coverslipped using DAKO-Mounting-Medium (DAKO, Germany). Images were captured with a Zeiss Axioplan epi-fluorescence microscope connected to a Zeiss Axiovision CCD camera and Zeiss AxioVision 4.8 software.

2.4. Morphometric analysis of microvessels (RECA-1 and EBA)

Data obtained from eight longitudinally sectioned spinal cord blocks per group were used for morphometric analyses. Transverse sections from the remaining four spinal cord blocks were used for qualitative descriptions. Quantification of RECA-1- and EBA-immunoreactive microvessels was based on the examination of 4 representative longitudinal sections spaced 250 μm apart per spinal cord sample and group (i.e. 32 sections per group). The percentage area occupied by RECA-1- and EBA-immunoreactive microvessels within defined areas of interests (AOIs, 225 $\mu\text{m} \times 175 \mu\text{m}$) at the rostral-, medial- and caudal interfaces in lesion-only (figure 1(A)) and collagen scaffold-implanted tissues (figure 1(B)) was calculated from images of uniform exposure times and thresholding using the 'analyse particles' function of ImageJ® (as described previously [30–32]). The same analyses were also made from AOIs from the contralateral, non-lesioned side of the spinal cord which acted as internal controls. Additionally, AOIs within the collagen scaffold at rostral, middle and caudal positions were also measured (figure 1(B)).

2.5. Statistical analyses

Quantitation of RECA-1- and EBA-immunoreactive microvessels was presented as mean \pm standard error



of the mean (SEM) of all AOIs and all examined sections. The pooled and overall data were compared by using the paired and unpaired Student's *t*-test. *P*-values of 0.05 or less were considered as statistically significant. All statistical analyses were calculated by GraphPad Prism 4 and were graphically represented as mean \pm SEM. Asterisks (*) were used to indicate statistical significance.

3. Results

Dark-field images and DAPI nuclear counterstains were used to demonstrate some of the morphological details including a clear delineation of the edge of the lesion/implantation site (figures 1(C), (D) and (F), (G)). In lesion-only animals, numerous fluid-filled cystic cavities were regularly observed throughout the

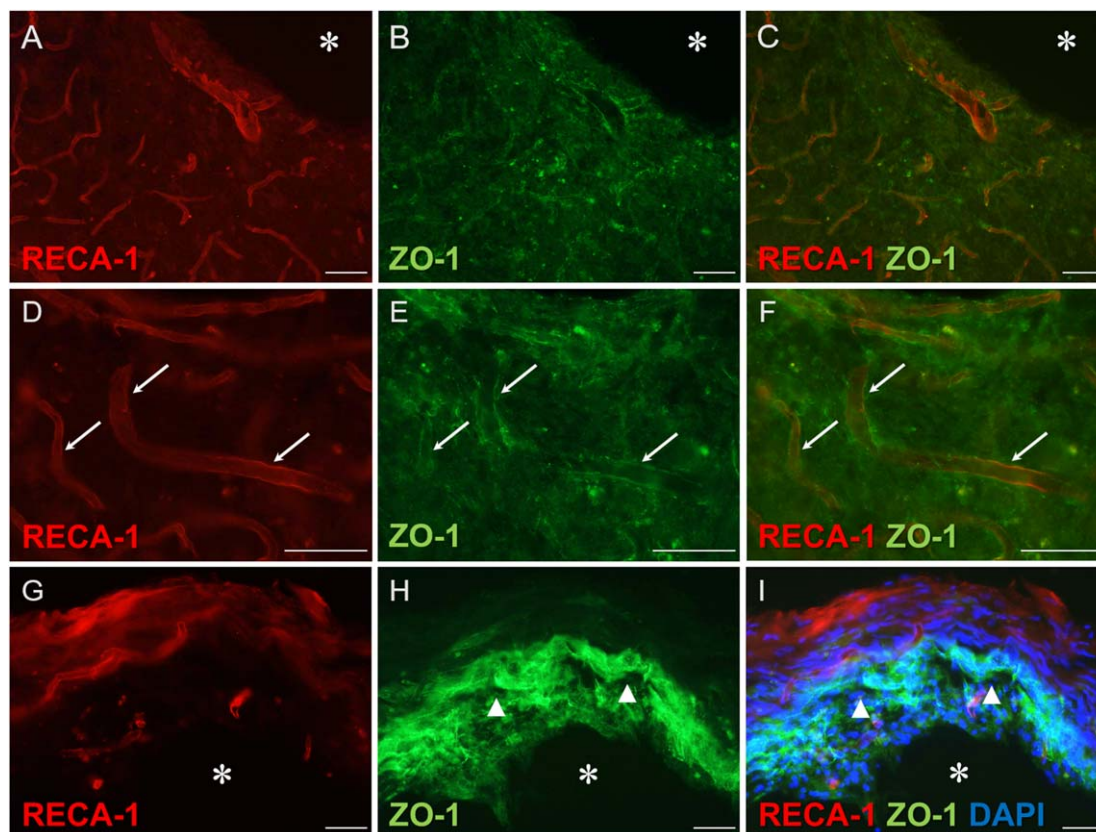


Figure 2. (A)–(I) Longitudinal sections of lesion-only spinal cords processed for RECA-1- and ZO-1-immunoreactivity at 10 weeks post-surgery. (A) An increased density of RECA-1-immunoreactive microvessels could be detected near the interface to the cystic cavity in lesion-only animals (asterisks, (A)–(C), but see also figure 4(A) for quantitative data). (B) and (C) These microvessels were double-immunoreactive for tight junction protein, ZO-1, which is better seen at high magnification (arrows, (D)–(F)). (G)–(I) Tight junction protein, ZO-1, was not only present on RECA-1-immunoreactive endothelial cells but also formed a part of a lateral tissue bridge between the dura mater and the main cystic cavity (asterisks, (G)–(I)) and arrowheads, (H)–(I)). The lateral tissue-bridge, which was also densely occupied by DAPI-labelled nuclei, was, in parts, strongly ZO-1-immunoreactive (arrowheads in H and in overlay I). Scale bars: 50 μ m.

lesion site (e.g. asterisks, figures 1(C)–(E)), in parts divided by trabeculae of scarring tissue and highlighted at the lateral-most edge by a cell rich region (including the dura mater), as indicated by the numerous DAPI-positive nuclei (arrowheads in figure 1(D)). NF200-positive host axons were often seen following the lateral-most tissue bridge or even sometimes following the trabeculae (e.g. arrowheads and arrow, figures 1(C)–(E)). In stark contrast to this, the collagen scaffold-implanted lesion sites demonstrated the formation of a transition zone around the rostral-, medial- and caudal implant-host interfaces that was often revealed as a dark band within the dark-field images and was occupied by densely packed DAPI-labelled nuclei (e.g. area between the dotted lines, figures 1(F)–(H)). Occasionally, scattered NF200-positive axons could be seen traversing the transition zone and entering the periphery of the implanted collagen scaffold (arrows in figure 1(H)). However, in most immunohistochemical sections, the transition zone was devoid of axonal profiles.

The distribution of blood vessels, as revealed by RECA-1-immunohistochemistry, demonstrated the clear disparity in density between normal grey- and

white matter (supplementary figures 1(A), (B) is available online at stacks.iop.org/BMM/15/015012/mmedia). However, in the spared tissue adjacent to the rostral-, medial- and caudal interfaces of the lesion-only group, an increased density of microvessels (in comparison to normal white matter) was observed (e.g. figure 2(A), but see also figure 4(A) for quantification). All these RECA-1-positive vessels were double-immunoreactive for the tight junction protein, ZO-1 (figures 2(A)–(C), also seen at higher magnification in figures 2(D)–(F)). Surprisingly, ZO-1-immunoreactivity was not only associated with RECA-1-immunoreactive blood vessels (figures 2(G)–(I)) but was also intensely present in a band of cells that formed part of the lateral tissue bridge, located between the large cystic cavity at the lesion epicentre and the medial surface of the dura mater (indicated by arrowheads, figures 2(H)–(I)).

The implanted type-I collagen scaffold demonstrated close contact with the lesioned host spinal cord when viewed by dark-/bright-field microscopy (e.g. figures 3(A), (E)) and as reported earlier, reduced the incidence of cavitation at the lesion site (data not shown, [30–32]). Angiogenesis had clearly taken place,

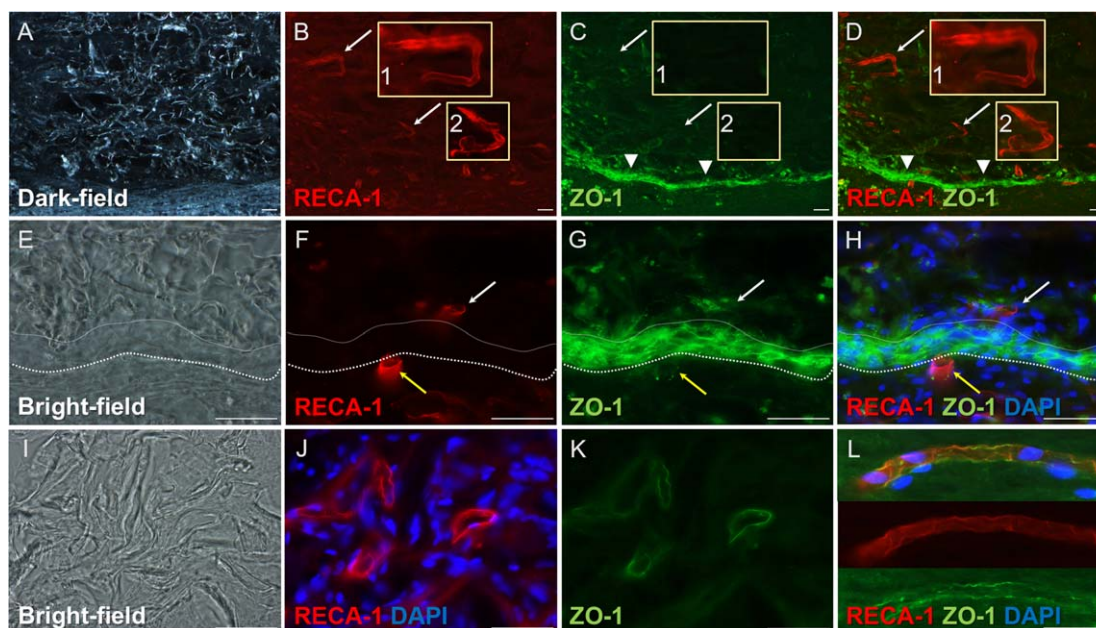
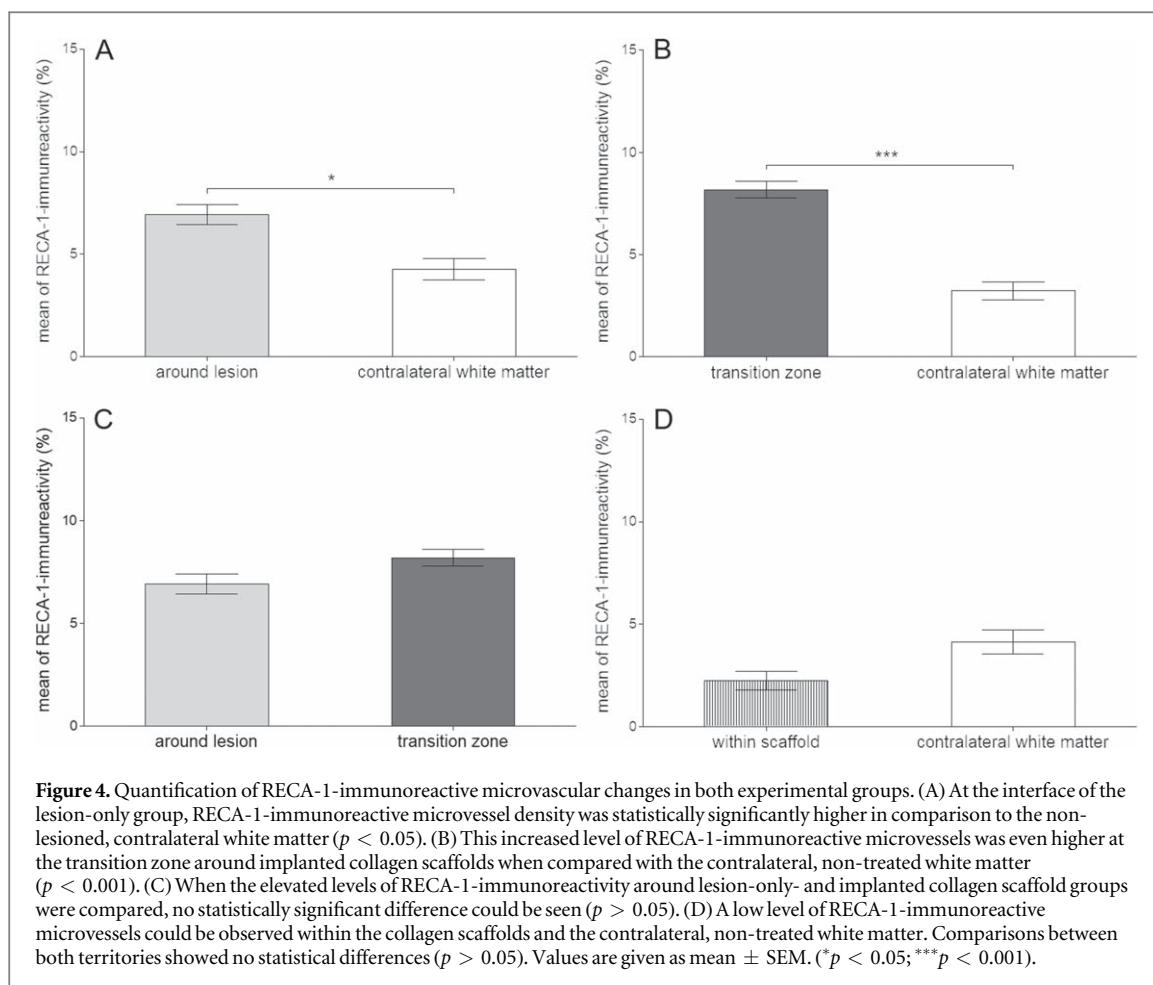


Figure 3. Longitudinal sections of implanted collagen scaffolds at 10 weeks post-surgery: RECA-1- and ZO-1-immunoreactivity. (A) The internal framework of the implanted collagen scaffold could be seen by dark-field microscopy. (B) RECA-1-immunoreactive microvessels deep within the collagen scaffolds indicated that angiogenesis had taken place (arrows, and higher magnification in insert 1 and 2). (C) Many of these vessels were not associated with tight junction protein, ZO-1 (see arrows and higher magnification inserts 1 and 2). (D) Overlay of B and C confirms the lack of co-localisation. Interestingly, an intense ZO-1-immunoreactive band of overlapping cells and processes could be detected at the rostral-, medial- and caudal transition zones (e.g. arrowheads, (C) and (D)). (E) Bright-field microscopy of the transition zone (between dotted lines, also indicated in (F)–(H)) appeared to act as a ‘water-shed’ for RECA-1-/ZO-1-immunoreactivity. While RECA-1-immunoreactive microvessels on the side of the spared spinal cord tissue were associated with tight junction protein ZO-1 (yellow arrow, (F)–(H)), vessels on the scaffold side of the transition zone were often not ZO-1-immunoreactive (white arrow, (F)–(H)). Strongly ZO-1-immunoreactive cellular processes and DAPI-labelled nuclei occupied the transition zone (between dotted lines in E, G and F). Although many of the newly formed RECA-1-immunoreactive microvessels within the collagen scaffold (I), (J) were not associated with tight junction protein, ZO-1, some vessels were clearly double labelled but showed a more uniform distribution throughout the whole endothelial cells (K) as could also be seen in baseline stains of the healthy, contralateral white matter (L). Scale bars: 50 μ m.

as indicated by the presence of RECA-1-immunoreactive vessels deep within the scaffolds (arrows in figure 3(B)). In contrast to the vessels within spinal cord grey- and white matter, many of the RECA-1-immunoreactive vessels within the collagen scaffolds were not associated with ZO-1-immunoreactive tight junctions (e.g. arrows in figures 3(C), (D) and at higher magnification in the inserts 1 and 2, see also supplementary figure 1(C) for an example of RECA-1/ZO-1-positive blood vessel within the contralateral, non-lesioned white matter). Furthermore, an intensely ZO-1-immunoreactive band of overlapping cells and processes could be observed at the rostral-, medial- and caudal transition zones that often surrounded the type-I collagen scaffold (e.g. arrowheads at the medial implant-host tissue transition zone of figures 3(C) and (D), also delineated by the dotted lines at higher magnification in figures 3(E)–(H)). The transition zone appeared to act as a type of ‘water-shed’ for RECA-1/ZO-1-immunoreactivity: RECA-1/ZO-1-positive vessels being located on the spared spinal tissue side of the transition zone (e.g. yellow arrow, figures 3(F)–(H)), while the vessels on the scaffold side of the transition zone were not (white arrow, figures 3(F)–(H)). Although many of the RECA-1-positive blood vessels that formed within the scaffold were not immunoreactive for the tight junction protein, ZO-1, some vessels

were positive but with the immunoreactivity being more uniformly distributed throughout the endothelial cells (figures 3(I)–(K)). This was also seen in control microvessels located in longitudinal sections of the contralateral, non-lesioned spinal cord white matter (e.g. figure 3(L)).

Quantitative morphometric analysis of RECA-1-immunoreactivity close to the interface of the lesion-only group confirmed that the blood vessel density was significantly higher than that of the contralateral, non-lesioned white matter ($p < 0.05$, figure 4(A)). This increase in the density of RECA-1-positive blood vessels showed an even greater level of statistical significance at the transition zone of the scaffold-implanted group when compared to the contralateral, non-lesioned white matter ($p < 0.001$, figure 4(B)). No significant difference was seen, however, between the amounts of RECA-1-staining around the lesion-only- and the scaffold-implanted interfaces ($p > 0.05$, figure 4(C)). Comparison of RECA-1-staining observed within the scaffold with that observed in the contralateral, non-lesioned white matter tracts revealed that both regions had similarly low amounts of microvessels and that there was no significant difference between them ($p > 0.05$, figure 4(D)).



An antibody directed against EBA was used as a morphological indicator of the functional maturity of blood vessels and for the establishment of the BSB [36, 37]. In lesion-only samples, ZO-1- and EBA-immunoreactive microvessels (figures 5(A) and (B), arrow in B, but also figure 5(C), arrow in insert) in the interface area were co-localised with ZO-1-immunoreactivity. A DAPI-positive cell-band was never observed at the medial interface of lesion-only samples (figure 5(D)). As mentioned earlier, the lateral tissue bridge of the lesion-only samples was often highlighted as a band of overlapping ZO-1-immunoreactive cells and processes. In some cases, the layer of cells in these regions were only 1–2 cells thick and even appeared discontinuous in places (figures 5(E)–(G)). A relatively frequent observation in such samples was the appearance of clusters of ZO-1-immunoreactive cells that were closely apposed to blood vessels, giving a ‘rose-like’ formation when cut in a plane that was transverse to the trajectory of the vessel (figures 5(E)–(G), and double arrows at higher magnification in figure 5(H)). However, not all vessels were coated by dense clusters of such cells, even when lying immediately adjacent to the cell encrusted vessels (single white arrow in figures 5(F), (H)).

The transition zone around the implanted collagen scaffolds (as indicated between the two dotted lines of figures 5(I)–(O)) contained variable numbers

of ZO-1-positive fibroblast-like cells that were associated with numerous EBA-immunoreactive microvessels (figure 5(J), see also figure 6(A) (for lesion-only interface quantification) and B (for collagen scaffold quantification)), however the number of EBA-immunoreactive vessels was significantly lower than the total number of vessels in that specific area (as indicated by RECA-1-staining, figure 6(B)). A very small number of EBA-immunoreactive vessels were also detected that were within the framework of the implanted collagen scaffolds (arrows in figure 5(J), see also figure 6(C) for quantification). Similar to the observations with RECA-1-immunoreactive blood vessels, the majority of the EBA-immunoreactive microvessels within the scaffold were also devoid of any endothelial ZO-1-positive tight junctions (figures 5(J)–(P), see also figure 6(C), $p < 0.01$) suggesting a delayed or slowed maturation.

To achieve a better characterisation of the range of cellular/vascular events and interactions taking place in and around the lesion/implanted scaffold areas, transverse cryosections were exposed to different combinations of antibodies recognising vimentin, ZO-1, EBA, Aqp-4, GFAP and RECA-1. In lesion-only samples, the cells lining the cystic cavities appeared to be variable: the lateral-most lining of the main cystic cavity was lined by intensely vimentin- and ZO-1-immunoreactive (and Aqp-4-negative) fibroblast-like

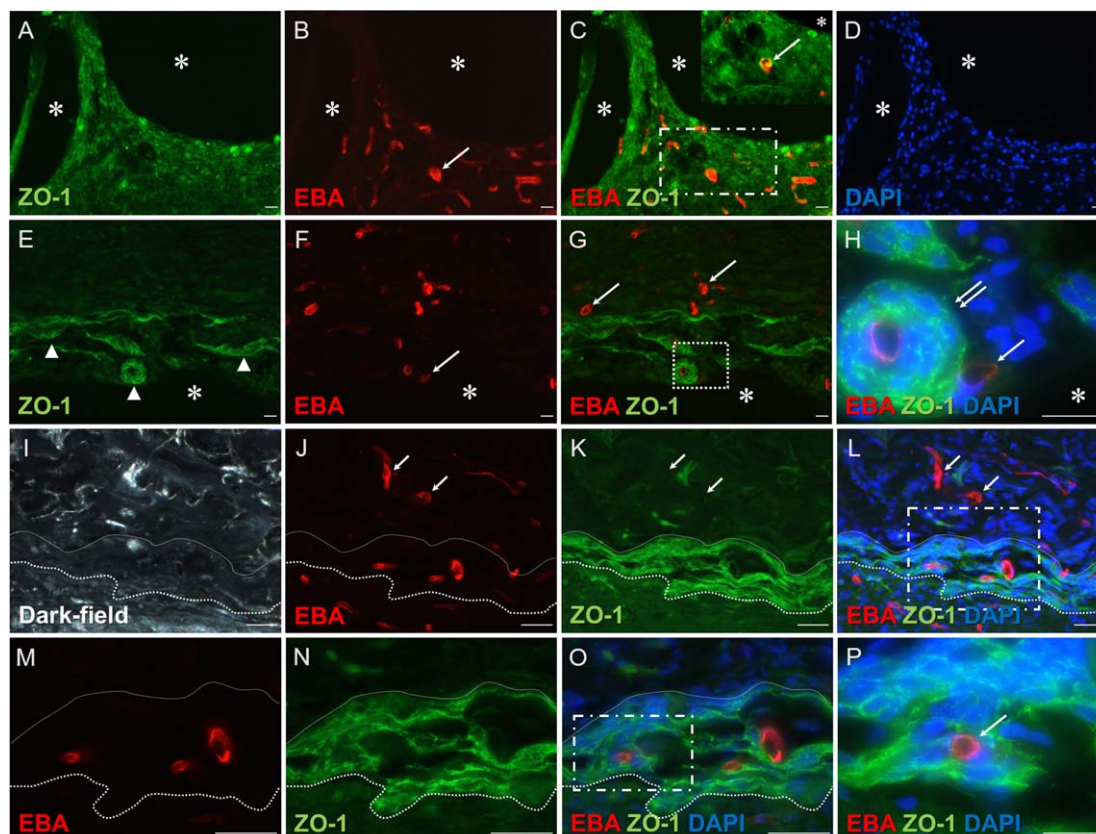


Figure 5. Longitudinal sections of lesion-only animals and implanted collagen scaffolds at 10 weeks post-surgery: EBA- and ZO-1-immunoreactivity. (A) The interface to the cystic cavity and lesion (asterisks, (A)–(H)) demonstrated tight junction protein ZO-1-positivity in EBA-positive vessels (compare (A)–(C)). (B) An anti-EBA antibody was used to detect mature CNS-microvessels. In lesion-only sections, EBA-immunoreactive microvessels were associated with tight junction protein ZO-1 (arrow in B, overlay of A and B in C, higher magnification insert C, arrow). (D) The interface-territory around cystic cavities could be seen. (E) The lateral tissue bridge, next to the cystic cavity (asterisks, (E)–(H)) showed a loose band of partially overlapping ZO-1-immunoreactive cells and processes (arrowheads). A common observation was the appearance of clusters of ZO-1-immunoreactive cells in ‘rose-like’ formations around blood vessels (E)–(G). In the centre of these ‘rose-like’ formations, an EBA-immunoreactive microvessel could be observed (dashed box in G, higher magnification in H, double arrow). Although many EBA-immunoreactive microvessels within the reconstructed and thickened dura mater were present, these were not associated with ZO-1-immunoreactivity (arrows). (H) Interestingly, some EBA-immunoreactive microvessels, despite being located next to the clustered ZO-1-positive cells were devoid of clusters (single arrow in F and same indicated vessel in H, at higher magnification). Scale bars. (I) The transition zone of the scaffold-implanted group also included some EBA-immunoreactive microvessels (between two dotted lines in J). A low number of EBA-immunoreactive microvessels could also be observed within the scaffold (arrows, J and L, but also compare with figure 6(B) for quantification). Interestingly, these microvessels were devoid of any ZO-1-immunoreactive tight junctions (arrows, K and L). (M)–(P) At higher magnification of the dashed box in L. Several EBA-immunoreactive microvessels could be seen passing through the ZO-1-immunoreactive transition zone (between dotted lines M–O) of collagen scaffold implanted group. (P) The ZO-1-positive cells often formed close associations with the EBA-positive vessel walls (arrow). Scale bars: (A)–(H), (P): 20 μm ; (I)–(O): 50 μm .

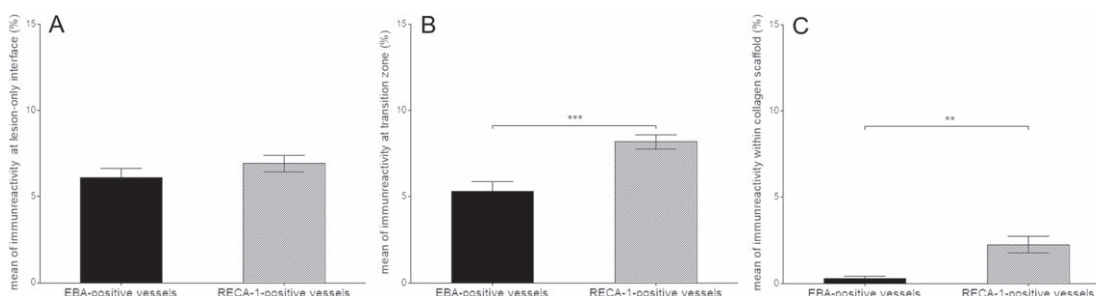


Figure 6. Quantification and statistical comparison of EBA- and RECA-1-immunoreactive microvascular changes in both experimental groups. (A) At and around the interface to the lesion-only group, no statistically significant difference could be demonstrated in the amount of EBA- and RECA-1-immunoreactive microvessels ($p > 0.05$). (B) In contrast to the lesion-only interface, there was a statistically significant decrease in the amount of EBA- in and around the transition zone of collagen scaffold implants in comparison to RECA-1-immunoreactive microvessels ($p < 0.001$). (C) This significant reduction of EBA-immunoreactive microvessels in comparison to RECA-1-positive microvessels was even more pronounced within the collagen scaffolds ($p < 0.01$). This apparent lack of EBA-immunoreactivity suggests a delayed or incomplete vessel maturation. Values are given as mean \pm SEM. (** $p < 0.01$; *** $p < 0.001$).

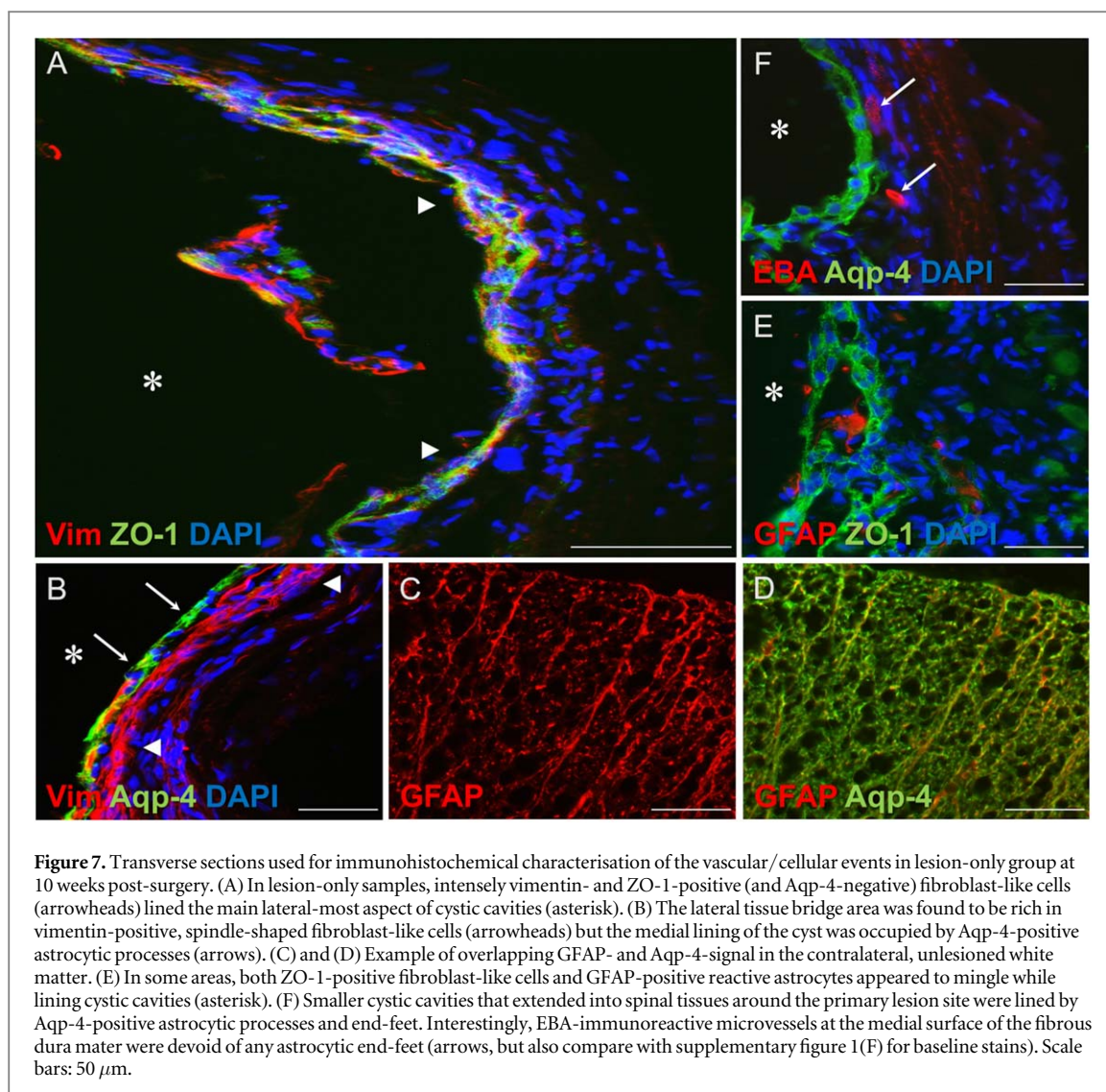


Figure 7. Transverse sections used for immunohistochemical characterisation of the vascular/cellular events in lesion-only group at 10 weeks post-surgery. (A) In lesion-only samples, intensely vimentin- and ZO-1-positive (and Aqp-4-negative) fibroblast-like cells (arrowheads) lined the main lateral-most aspect of cystic cavities (asterisk). (B) The lateral tissue bridge area was found to be rich in vimentin-positive, spindle-shaped fibroblast-like cells (arrowheads) but the medial lining of the cyst was occupied by Aqp-4-positive astrocytic processes (arrows). (C) and (D) Example of overlapping GFAP- and Aqp-4-signal in the contralateral, unlesioned white matter. (E) In some areas, both ZO-1-positive fibroblast-like cells and GFAP-positive reactive astrocytes appeared to mingle while lining cystic cavities (asterisk). (F) Smaller cystic cavities that extended into spinal tissues around the primary lesion site were lined by Aqp-4-positive astrocytic processes and end-feet. Interestingly, EBA-immunoreactive microvessels at the medial surface of the fibrous dura mater were devoid of any astrocytic end-feet (arrows, but also compare with supplementary figure 1(F) for baseline stains). Scale bars: 50 μ m.

cells, as part of the lateral connective tissue bridge (arrowheads in figure 7(A)). In contrast, cells lining the smaller cystic cavities that extended into spinal tissues around the primary lesion site demonstrated a different phenotype, being Aqp-4-positive (figure 7(B)), a well-established marker of astrocytes, their processes and end-feet, as seen by the overlapping GFAP- and Aqp-4-signal in the contralateral unlesioned white matter regions (figures 7(C), (D)). In other areas, both ZO-1-positive fibroblast-like cells and GFAP-positive reactive astrocytes appeared to share the role of lining the cystic cavities (figure 7(E)). However, ZO-1-immunoreactive cells lining the medial interface to the cystic cavities were never observed in lesion-only animals (see supplementary figure 1(D)). Situated between the astrocytic lining of the cysts and the fibrous dura mater were numerous EBA-immunoreactive microvessels that were devoid of any astrocytic end-feet (figure 7(F), arrows, but also see supplementary figure 1(D), F for baseline distribution of Aqp-4 around RECA-1/EBA-positive white matter blood vessels). This area was also found to be rich in vimentin-positive, spindle-shaped fibroblast-like cells (arrowheads, figure 7(B)).

Although the tightly packed, overlapping, vimentin-positive, fibroblast-like cells that occupied the transition zone were also intensely ZO-1-immunoreactive (arrowheads, figures 8(A), (B)), a large number of similarly vimentin-positive, spindle-shaped cells could also be seen deeply penetrating the porous framework of the collagen scaffold, where they had scattered and adopted a loosely packed, generally longitudinally orientated morphology. These fibroblast-like cells were clearly not ZO-1-immunoreactive (small arrows, figure 8(A)). A high magnification of the transition zone demonstrated bipolar vimentin-positive cells with multiple tight junctions (figure 8(B), arrowheads, followed by vimentin-only-positive fibroblast-like cells, with bipolar, thin-long processes). Frequently, vimentin-positive fibroblast-like cells accumulated as tightly packed clusters at the transition zone, generating a sharp boundary with the Aqp-4-immunopositive reactive host astrocytic-territory (figure 8(C), arrowheads, see also figures 7(C), (D) for baseline GFAP- and Aqp-4-stains in spinal cord white matter). Although RECA-1-immunoreactive microvessels were found within the scaffolds, fewer EBA-

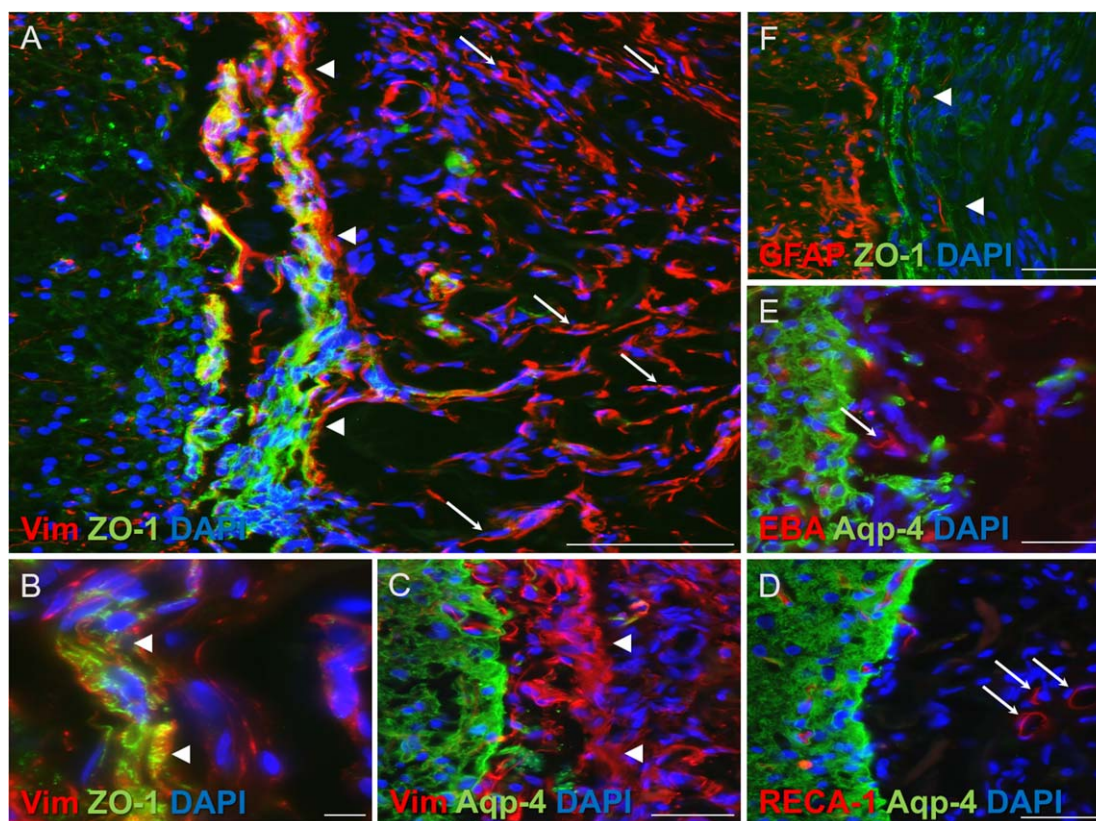


Figure 8. Transverse sections used for immunohistochemical characterisation of the vascular/cellular events in collagen scaffold implanted group at 10 weeks post-surgery. (A), (B) At the transition zone of the implanted collagen scaffold, tightly packed, overlapping, vimentin-positive, fibroblast-like cells could be observed, which were also intensely ZO-1-immunoreactive (arrowheads, also at high power in B). Similarly, vimentin-positive, spindle-shaped cells could be seen within the porous framework of the collagen scaffold. The fibroblast-like cells within the scaffolds were clearly not ZO-1-immunoreactive (arrows in A). (C) The formed connective tissue barrier was of varying thickness between the Aqp-4-positive reactive astrocytic processes of the surrounding host spinal cord and the edge of the scaffold (arrowheads). Although RECA-1- (arrows in D) and rarely EBA-immunoreactive microvessels (arrow in E) could be found within the scaffolds, hardly any Aqp-4-immunoreactive astrocytic processes or end-feet could be detected around these vessels (also compare with supplementary figures 1(E) and (F) for baseline stains). (F) The ZO-1-immunoreactive transition zone and the GFAP-positive scarring astrocytes constituted a double-fibroadhesive/astroglial barrier that isolated the collagen scaffold from most of the host neural cells (arrowheads, but also compare figures 7(C) and (D) for baseline GFAP- and Aqp-4-stains in spinal cord white matter). Scale bars: (A) and (C)–(F): 50 μm ; (B): 10 μm .

immunoreactive vessels were seen (arrows in figures 8(D) and (E), respectively) and hardly any accompanying Aqp-4-immunoreactive astrocytic end-feet could be detected within the territory of the collagen scaffold. As mentioned above, Aqp-4-immunoreactive astrocytic territory could be seen by the sharp boundary that terminated at the edge of the transition zone (figures 8(C)–(E)). The establishment of such sharply demarcated territories strongly suggests that the ZO-1-positive fibroblast-like cells and GFAP/Aqp-4-positive reactive astrocytes may have properties of strong mutual repulsion (figures 8(C)–(F)).

4. Discussion

It is widely accepted that a combination of intervention strategies is likely to yield the most successful tissue repair and functional recovery after SCI [38, 39]. Significant advances continue to be made in developing bioengineered scaffolds with orientated, micro- or nanostructured topographies that can support

regenerative axonal growth across the hostile territory of the cystic cavity-laden lesion site (e.g. [18, 40–42]).

This investigation demonstrated novel aspects of scaffold-host tissue interactions following the implantation of type-I collagen scaffolds into unilateral resection injuries of the adult rat cervical spinal cord. Neovascularisation of the scaffolds was observed in these long-term (i.e. 10 wps) studies, but there was little evidence of microvessel maturation in the context of re-establishing the BSB. Relatively few endothelial cells of the newly formed vessels within the scaffold showed any expression of the tight junction protein, ZO-1 or of EBA. However, ZO-1-immunohistochemistry revealed intense staining of the vimentin-positive fibroblast-like cells as part of the host scarring response that we had previously reported as surrounding the implanted scaffold as a band or transition zone of encapsulating cells [32].

In the present experimental model, the type-I collagen scaffold was implanted to bridge a 2 mm unilateral resection injury of the lateral cervical white

matter tract of the adult rat spinal cord. It is noteworthy that the implanted scaffold supported new microvessel formation, quantitatively similar to that seen in normal spinal cord white matter (as shown by comparison to the contralateral, uninjured lateral funiculus). In the context of axonal growth and tissue repair, a number of studies have demonstrated a close spatial relationship between newly formed blood vessels and axonal regeneration [34, 40, 43–45]. It may be that strategies that increase microvessel density within the collagen scaffold would support greater axon growth, as suggested by others [45, 46]. The identification of angiogenesis within implanted scaffolds RECA-1 or type-IV collagen immunohistochemistry only provides partial information about the status of the vessels. Other indicators of vessel functionality and integrity within CNS implants are of substantial importance since CNS tissue is known to be a ‘privileged’ tissue [47]. An intact BSB is pivotal for the function of the spinal cord and is supported by the presence of non-fenestrated capillary endothelial cells, a basal lamina, pericytes and astrocytic end-feet [48]. The presence of tight junctions, typically composed of key molecules such as claudin-5, occludin and ZO-1, is a fundamental indicator of the formation and maintenance of a functional BSB [48–50]. Any deficiency or lack of expression of these proteins suggests significant disruption of tight junctions and it is widely accepted that reduced levels of endothelial ZO-1 are associated with reduced vessel barrier-function in a number of neurological disorders (e.g. [51]). The results of the present study showed a similar extent of increased angiogenesis (RECA-1-immunoreactive microvessels) around the interface of long-term lesion-only and collagen scaffold implanted animals. Others have reported that angiogenic events start as early as 3–4 d post-injury [52] and that increased numbers of vessels may be achieved by 7 d [53]. The present study also showed that the vast majority of the vessels that formed within the lesion site and within the collagen scaffold of implanted animals lacked ZO-1- and EBA-immunoreactivity, suggesting an inability to form fully mature or functional vessels in the context of reformation of a BSB. To assess possible reasons underlying the formation of such blood vessels, their spatial relationship with astrocytic profiles was investigated. Since GFAP-immunoreactivity does not define the complete territory occupied by astrocytes [54], Aqp-4-immunohistochemistry was used. Aqp-4 is exclusively expressed by rodent spinal cord astrocytes [55, 56] and this membrane-bound water channel is normally located on astrocytic end-feet in close apposition to CNS-microvessels [57]. Interference of the barrier role of astrocytic end-feet around microvessels has been demonstrated to result in enhanced vessel permeability [58]. It was clear that host Aqp-4-positive astrocytic profiles largely failed to penetrate the implant and therefore could not be found in association with the blood vessels within the scaffold. It is likely that

this contributed to the lack of ZO-1- and EBA-immunoreactivity on these vessels and that, as a consequence, they remained permeable to certain blood-borne proteins that are normally excluded by the BSB. However, this suggestion needs to be confirmed by further studies.

An inability of reactive astrocytic processes to penetrate the epicenter of the lesion site appears to be a consistent observation in a number of experimental models of CNS injury (including compression and transection injuries of the spinal cord, and ischemic stroke injuries within the brain) [59–61]. Cha and colleagues demonstrated the development of a dense fibrotic scar at the lesion site in models of stroke injury. This prevented astrocytic penetration and, from approximately 2 weeks post-injury, acted as a barrier that prevented inflammatory cell encroachment into adjacent spared CNS tissues as well as limiting the consequences of enhanced blood vessel permeability on adjacent tissue survival. The authors demonstrated that blood vessels within the lesion site remained permeable to serum proteins over a number of weeks but that the forming fibrotic scar acted as a physical barrier to the spread of exuded serum proteins. A-kinase anchoring protein 12 (AKAP12) was shown to play a pivotal role in such barrier formation [60].

The lack of ZO-1- or EBA-immunoreactivity on newly formed scaffold microvessels was a site (or location) specific phenomenon, since newly formed vessels at the medial interface of lesion-only animals and the fibroblast-rich transition zone after scaffold implantation both demonstrated robust Aqp-4-immunoreactivity around EBA- and ZO-1-immunoreactive blood vessels. Although these observations support the well-established relationship between endothelial cells and astrocytic profiles in BSB formation [48, 57], there were other regions of the sections (e.g. sub-dural regions, the ZO-1-immunoreactive transition zone surrounding the implant and vessels surrounded by ZO-1-positive clusters of fibroblast-like cells) that exhibited EBA-immunoreactive blood vessels. These were neither ZO-1-immunoreactive nor supported by closely apposed astrocytic profiles. Others have reported the presence of EBA-immunoreactive blood vessels within the meninges, in astrocyte-free territories that were close to the glia limitans of the adult rat brain [62, 63]. Vessels located further away from the glia limitans showed progressively weaker EBA-immunoreactivity which suggested that diffusible astrocyte-derived factors may be responsible for the induction of EBA in endothelial cells that were not in direct contact to CNS astrocytes but were located close to them [62, 63]. This suggestion might also explain the presence of occasional EBA-positive endothelial cells that were observed within the transition zone and implanted scaffold of the present study.

The present study also revealed the novel observation that not all regions of the cystic cavities were lined

by Aqp-4-positive astrocytic profiles, but included cell profiles that were intensely immunoreactive for vimentin and ZO-1. The involvement of astrocytic profiles has been suggested to reflect the reformation of the glia limitans [57, 64, 65]. It is possible that the vimentin/ZO-1-positive cells identified at the lateral edge of the main cystic cavity, adjacent to the lateral tissue bridge could be the same as, or similar to, the fibroblast-like cells located at the implant-host interface of the collagen scaffolds. In support of this, others have demonstrated that collagen and its degradation products is chemotactic to fibroblasts [66]. It may be that the collagen of the dura mater and of the implanted scaffold acted as a primary substrate for cell migration by these scarring, vimentin/ZO-1-positive fibroblast-like cells.

The use of an anti-ZO-1 antibody in the characterisation of BSB reformation in this study revealed a novel aspect of the fibrotic scarring in response to implanted collagen scaffolds. The vimentin-positive fibroblast-like cells that had previously been found to form a band of overlapping cells and processes of variable thickness around the implanted scaffold [32] were also observed to be intensely ZO-1-immunoreactive. Histological evidence of encapsulating connective tissue responses to implanted collagen hydrogels have been reported by others in experimental rat SCI. The presence of fibroblasts in and around the implants was associated with the ingrowth of blood vessels from surrounding connective tissue and progressive compartmentalisation or encapsulation [67]. A similar fibrotic scarring response around implanted, microstructured type-I/III collagen scaffolds in experimental models of rat SCI was also described [27, 28]. In those studies, a range of growth-factors, drugs or axon growth-promoting cells were combined with the scaffolds, but little evidence of axonal growth through the scaffolds could be found. The authors suggested that invading meningeal fibroblasts were responsible for the fibrotic scarring response. This suggestion has, more recently, been confirmed by our previous study, which showed that scarring cells of the transition zone were vimentin-positive, GFAP-negative and S100-negative [32]. The present study has extended the characterisation of these cells by demonstrating the rich and highly localised expression of the tight junction protein, ZO-1, in this region. This supports the notion that the formation of tight junctions between fibroblasts (or fibroblast-like cells) plays an important role in the wound healing response of a wide range of tissues (as recently reviewed by Shi and co-workers [68]).

Our study demonstrated the formation of two layers of scarring tissue around the implant; an innermost layer of fibroblast-like cells (vimentin/ZO-1-positive and GFAP/Aqp-4-negative) surrounded by the astroglial scar (GFAP/Aqp-4-positive, ZO-1-negative). This pattern shows a striking resemblance to the meningeal fibroblast/connective tissue scarring that

develops over a number of weeks around experimental ischemic/stroke injuries and was shown to be important in limiting inflammation [60]. Interestingly, data from other groups also indicated a spatial separation of reactive host astrocytes from the edge of an implanted (synthetic or natural) polymer bioscaffold (including biodegradable poly-hydroxybutyrate, chitosan and/or alginate scaffolds, all of these polymers being foreign to CNS [69, 70]). While some investigators failed to define the cellular contents of the space between the implant and the reactive host astrocytes, others clearly demonstrated that it contained DAPI-labelled, GFAP-negative cells [69]. These observations appear to be similar to those presented in the present investigation, provoking the suggestion that the novel aspect of the scarring response to implanted collagen scaffolds may also be involved in the host responses to a wider range of implants. However, this suggestion needs to be tested in future studies.

The scarring response of damaged CNS tissues (particularly in the context of implanted biomaterials, scaffolds or electrodes) has often focused on the glial aspect of scarring (e.g. [71, 72]). However, over recent years a better characterisation of the cellular and molecular aspects of scarring (including both glial and fibrotic scarring) has highlighted numerous potential targets for therapeutic intervention (e.g. [40, 73–75]). In this context, the cells critically involved in forming the fibrotic scar after SCI have been extended from meningeal fibroblasts to include blood vessel-associated fibroblasts and pericytes [76, 77]. It is of critical importance that any applied intervention only interferes with the detrimental aspects (e.g. encapsulation) of such scarring responses, since these are intended to facilitate greater implant-host integration and improve functional tissue repair. Such strategies will likely be incorporated into future combinational approaches in tissue engineering and regenerative medicine designed to promote functional recovery after severe traumatic SCI.

5. Conclusion

The present study showed that a bioengineered micro-porous collagen scaffold was capable of supporting an angiogenic response by the host spinal cord resulting in microvessel formation within the implant at a density appropriate for the cervical lateral white matter tracts that the implant replaced. Immunohistochemistry suggested that microvessel maturation was impaired, as indicated by the lack of (ZO-1-immunoreactive) endothelial tight junctions and of the EBA. This lack of microvessel maturation was associated with the failure of astrocytic profiles to penetrate the scaffold for any significant distance, which was in turn, likely to be due to the formation of a previously unidentified and intensely ZO-1-immunoreactive layer of overlapping fibroblast-like cells and processes

at the implant-host transition zone. These observations highlight the importance of striving to obtain a detailed characterisation of the cellular and molecular events that negatively influence implant-host integration. The targeted manipulation of these events will likely contribute to future combinational intervention strategies by improving scaffold integration and regenerative performance in traumatically injured spinal cords.

Acknowledgments

Dr. Ingo Heschel (Matricel GmbH, Herzogenrath, Germany) is gratefully acknowledged for providing the collagen scaffolds.

Ethical approval

Animal care and experimental procedures were carried out in accordance with the guidelines of the Belgian animal protection statute and were approved by the Belgium governmental ethical committee.

Funding

This research project is supported by the START-Program of the Faculty of Medicine, RWTH Aachen.

Conflicts of interest statement

The authors have no conflicts of interest to disclose.

ORCID iDs

Haktan Altinova  <https://orcid.org/0000-0002-1039-7553>

Tobias Führmann  <https://orcid.org/0000-0003-1857-4806>

References

- [1] Faulkner J R, Herrmann J E, Woo M J, Tansey K E, Doan N B and Sofroniew M V 2004 Reactive astrocytes protect tissue and preserve function after spinal cord injury *J. Neurosci.* **24** 2143–55
- [2] Fitch M T, Doller C, Combs C K, Landreth G E and Silver J 1999 Cellular and molecular mechanisms of glial scarring and progressive cavitation: *in vivo* and *in vitro* analysis of inflammation-induced secondary injury after CNS trauma *J. Neurosci.* **19** 8182–98
- [3] Fitch M T and Silver J 2008 CNS injury, glial scars, and inflammation: inhibitory extracellular matrices and regeneration failure *Exp. Neurol.* **209** 294–301
- [4] Hall E D and Springer J E 2004 Neuroprotection and acute spinal cord injury: a reappraisal *NeuroRx* **1** 80–100
- [5] Popovich P G, Wei P and Stokes B T 1997 Cellular inflammatory response after spinal cord injury in Sprague-Dawley and Lewis rats *J. Comp. Neurol.* **377** 443–64
- [6] Silver J and Miller J H 2004 Regeneration beyond the glial scar *Nat. Rev. Neurosci.* **5** 146–56
- [7] Ahuja C S et al 2017 Traumatic spinal cord injury-repair and regeneration *Neurosurgery* **80** S9–22
- [8] Rouanet C, Reges D, Rocha E, Gagliardi V and Silva G S 2017 Traumatic spinal cord injury: current concepts and treatment update *Arquivos Neuro-Psiquiatria* **75** 387–93
- [9] Kadoya K et al 2009 Combined intrinsic and extrinsic neuronal mechanisms facilitate bridging axonal regeneration one year after spinal cord injury *Neuron* **64** 165–72
- [10] Liu S, Schackel T, Weidner N and Puttagunta R 2017 Biomaterial-supported cell transplantation treatments for spinal cord injury: challenges and perspectives *Frontiers Cell. Neurosci.* **11** 430
- [11] Noble L J and Wrathall J 1989 Distribution and time course of protein extravasation in the rat spinal cord after contusive injury *Brain Res.* **482** 57–66
- [12] Oudega M, Bradbury E J and Ramer M S 2012 Combination therapies *Handbook Clin. Neurol.* **109** 617–36
- [13] Ahuja C S and Fehlings M 2016 Concise review: bridging the gap: novel neuroregenerative and neuroprotective strategies in spinal cord injury *Stem Cells Transl. Med.* **5** 914–24
- [14] Orr M B and Gensel J C 2018 Spinal cord injury scarring and inflammation: therapies targeting glial and inflammatory responses *Neurotherapeutics* **15** 541–53
- [15] Tam R Y, Fuehrmann T, Mitrousis N and Shoichet M S 2014 Regenerative therapies for central nervous system diseases: a biomaterials approach *Neuropsychopharmacology* **39** 169–88
- [16] Fuhrmann T, Anandakumaran P N and Shoichet M S 2017 Combinatorial therapies after spinal cord injury: how can biomaterials help? *Adv. Healthcare Mater.* **6** 1601130
- [17] Krishna V, Konakondla S, Nicholas J, Varma A, Kindy M and Wen X 2013 Biomaterial-based interventions for neuronal regeneration and functional recovery in rodent model of spinal cord injury: a systematic review *J Spinal Cord Med.* **36** 174–90
- [18] Koffler J et al 2019 Biomimetic 3D-printed scaffolds for spinal cord injury repair *Nat. Med.* **25** 263–9
- [19] Schoof H, Apel J, Heschel I and Rau G 2001 Control of pore structure and size in freeze-dried collagen sponges *J. Biomed. Mater. Res.* **58** 352–7
- [20] Bozkurt A et al 2007 *In vitro* assessment of axonal growth using dorsal root ganglia explants in a novel three-dimensional collagen matrix *Tissue Eng.* **13** 2971–9
- [21] Mollers S et al 2009 Cytocompatibility of a novel, longitudinally microstructured collagen scaffold intended for nerve tissue repair *Tissue Eng. A* **15** 461–72
- [22] Fuhrmann T, Hillen L M, Montzka K, Woltje M and Brook G A 2010 Cell-cell interactions of human neural progenitor-derived astrocytes within a microstructured 3D-scaffold *Biomaterials* **31** 7705–15
- [23] Bozkurt A et al 2009 *In vitro* cell alignment obtained with a Schwann cell enriched microstructured nerve guide with longitudinal guidance channels *Biomaterials* **30** 169–79
- [24] van Neerven S G et al 2014 Human Schwann cells seeded on a novel collagen-based microstructured nerve guide survive, proliferate, and modify neurite outgrowth *BioMed. Res. Int.* **2014** 493823
- [25] Joosten E A, Bar P R and Gispén W H 1995 481–90 Collagen implants and cortico-spinal axonal growth after mid-thoracic spinal cord lesion in the adult rat *J. Neurosci. Res.* **41** <https://doi.org/10.1002/jnr.490410407>
- [26] Spilker M H, Yannas I V, Kostyk S K, Norregaard T V, Hsu H P and Spector M 2001 The effects of tubulation on healing and scar formation after transection of the adult rat spinal cord *Restor. Neurol. Neurosci.* **18** 23–38
- [27] Cholas R, Hsu H P and Spector M 2012 Collagen scaffolds incorporating select therapeutic agents to facilitate a reparative response in a standardized hemisection defect in the rat spinal cord *Tissue Eng. A* **18** 2158–72
- [28] Cholas R H, Hsu H P and Spector M 2012 The reparative response to cross-linked collagen-based scaffolds in a rat spinal cord gap model *Biomaterials* **33** 2050–9
- [29] Snider S et al 2017 A novel composite type I collagen scaffold with micropatterned porosity regulates the entrance of phagocytes in a severe model of spinal cord injury *J. Biomed. Mater. Res. B Appl Biomater.* **105** 1040–53

- [30] Altinova H *et al* 2014 Functional improvement following implantation of a microstructured, type-I collagen scaffold into experimental injuries of the adult rat spinal cord *Brain Res.* **1585** 37–50
- [31] Altinova H *et al* 2016 Functional recovery not correlated with axon regeneration through olfactory ensheathing cell-seeded scaffolds in a model of acute spinal cord injury *Tissue Eng. Regen. Med.* **13** 585–600
- [32] Altinova H *et al* 2019 Fibroadhesive scarring of grafted collagen scaffolds interferes with implant-host neural tissue integration and bridging in experimental spinal cord injury *Regen. Biomater.* **6** 75–87
- [33] Figley S A, Khosravi R, Legasto J M, Tseng Y F and Fehlings M G 2014 Characterization of vascular disruption and blood-spinal cord barrier permeability following traumatic spinal cord injury *J. Neurotrauma* **31** 541–52
- [34] Bearden S E and Segal S S 2005 Neurovascular alignment in adult mouse skeletal muscles *Microcirculation* **12** 161–7
- [35] Raab S and Plate K H 2007 607–26 Different networks, common growth factors: shared growth factors and receptors of the vascular and the nervous system *Acta Neuropathologica* **113** <https://doi.org/10.1007/s00401-007-0228-3>
- [36] Sternberger N H and Sternberger L A 1987 Blood-brain barrier protein recognized by monoclonal antibody *Proc. Natl Acad. Sci. USA* **84** 8169–73
- [37] Loy D N, Crawford C H, Darnall J B, Burke D A, Onifer S M and Whittemore S 2002 Temporal progression of angiogenesis and basal lamina deposition after contusive spinal cord injury in the adult rat *J. Comp. Neurol.* **445** 308–24
- [38] Lu P and Tuszynski M H 2008 Growth factors and combinatorial therapies for CNS regeneration *Exp. Neurol.* **209** 313–20
- [39] Wang Y, Tan H and Hui X 2018 Biomaterial scaffolds in regenerative therapy of the central nervous system *BioMed. Res. Int.* **2018** 7848901
- [40] Hakim J S *et al* 2019 Combinatorial tissue engineering partially restores function after spinal cord injury *J. Tissue Eng. Regen. Med.* **13** 857–73
- [41] Gunther M I, Weidner N, Muller R and Blesch A 2015 Cell-seeded alginate hydrogel scaffolds promote directed linear axonal regeneration in the injured rat spinal cord *Acta Biomater.* **27** 140–50
- [42] Sun Y *et al* 2019 3D printing collagen/chitosan scaffold ameliorated axon regeneration and neurological recovery after spinal cord injury *J. Biomed. Mater. Res. A* **107** 1898–1908
- [43] Lopez-Dolado E, Gonzalez-Mayorga A, Gutierrez M C and Serrano M C 2016 Immunomodulatory and angiogenic responses induced by graphene oxide scaffolds in chronic spinal hemisectioned rats *Biomaterials* **99** 72–81
- [44] Madigan N N *et al* 2014 Comparison of cellular architecture, axonal growth, and blood vessel formation through cell-loaded polymer scaffolds in the transected rat spinal cord *Tissue Eng. A* **20** 2985–97
- [45] Rauch M F *et al* 2009 Engineering angiogenesis following spinal cord injury: a coculture of neural progenitor and endothelial cells in a degradable polymer implant leads to an increase in vessel density and formation of the blood-spinal cord barrier *Eur. J. Neurosci.* **29** 132–45
- [46] Wang L, Shi Q, Dai J, Gu Y, Feng Y and Chen L 2018 Increased vascularization promotes functional recovery in the transected spinal cord rats by implanted vascular endothelial growth factor-targeting collagen scaffold *J. Orthopaedic Res.* **36** 1024–34
- [47] Barker C F and Billingham R E 1977 Immunologically privileged sites *Adv. Immunol.* **25** 1–54
- [48] Bartanusz V, Jezova D, Alajajian B and Digicaylioglu M 2011 The blood-spinal cord barrier: morphology and clinical implications *Ann. Neurol.* **70** 194–206
- [49] Reinhold A K and Rittner H L 2017 Barrier function in the peripheral and central nervous system—a review *Pflugers Arch.: Eur. J. Physiol.* **469** 123–34
- [50] Zhong Z *et al* 2008 ALS-causing SOD1 mutants generate vascular changes prior to motor neuron degeneration *Nat. Neurosci.* **11** 420–2
- [51] Katsuno T *et al* 2008 Deficiency of zonula occludens-1 causes embryonic lethal phenotype associated with defected yolk sac angiogenesis and apoptosis of embryonic cells *Mol. Biol. Cell* **19** 2465–75
- [52] Ng M T, Stammers A T and Kwon B K 2011 Vascular disruption and the role of angiogenic proteins after spinal cord injury *Transl. Stroke Res.* **2** 474–91
- [53] Dray C, Rougon G and Debarbieux F 2009 Quantitative analysis by *in vivo* imaging of the dynamics of vascular and axonal networks in injured mouse spinal cord *Proc. Natl Acad. Sci. USA* **106** 9459–64
- [54] Bushong E A, Martone M E, Jones Y Z and Ellisman M H 2002 Protoplasmic astrocytes in CA1 stratum radiatum occupy separate anatomical domains *J. Neurosci.* **22** 183–92
- [55] Nestic O *et al* 2006 Acute and chronic changes in aquaporin 4 expression after spinal cord injury *Neuroscience* **143** 779–92
- [56] Oshio K, Binder D K, Yang B, Schecter S, Verkman A S and Manley G T 2004 Expression of aquaporin water channels in mouse spinal cord *Neuroscience* **127** 685–93
- [57] Verkman A S 2008 Mammalian aquaporins: diverse physiological roles and potential clinical significance *Expert Rev. Mol. Med.* **10** e13
- [58] Simard M, Arcuino G, Takano T, Liu Q S and Nedergaard M 2003 Signaling at the gliovascular interface *J. Neurosci.* **23** 9254–62
- [59] Brook G A *et al* 1998 Spontaneous longitudinally orientated axonal regeneration is associated with the Schwann cell framework within the lesion site following spinal cord compression injury of the rat *J. Neurosci. Res.* **53** 51–65
- [60] Cha J H *et al* 2014 AKAP12 mediates barrier functions of fibrotic scars during CNS repair *PLoS One* **9** e94695
- [61] Imperato-Kalmar E L, McKinney R A, Schnell L, Rubin B P and Schwab M E 1997 Local changes in vascular architecture following partial spinal cord lesion in the rat *Exp. Neurol.* **145** 322–8
- [62] Cassella J P, Lawrenson J G, Allt G and Firth J A 1996 Ontogeny of four blood-brain barrier markers: an immunocytochemical comparison of pial and cerebral cortical microvessels *J. Anat.* **189** 407–15
- [63] Cassella J P, Lawrenson J G, Lawrence L and Firth J A 1997 Differential distribution of an endothelial barrier antigen between the pial and cortical microvessels of the rat *Brain Res.* **744** 335–8
- [64] Rash J E, Yasumura T, Hudson C S, Agre P and Nielsen S 1998 Direct immunogold labeling of aquaporin-4 in square arrays of astrocyte and ependymocyte plasma membranes in rat brain and spinal cord *Proc. Natl Acad. Sci. USA* **95** 11981–6
- [65] Nestic O *et al* 2010 Aquaporins in spinal cord injury: the janus face of aquaporin 4 *Neuroscience* **168** 1019–35
- [66] Postlethwaite A E, Seyer J M and Kang A H 1978 Chemotactic attraction of human fibroblasts to type I, II, and III collagens and collagen-derived peptides *Proc. Natl Acad. Sci. USA* **75** 871–5
- [67] Gelderd J B 1990 80–92 Evaluation of blood vessel and neurite growth into a collagen matrix placed within a surgically created gap in rat spinal cord *Brain Res.* **511** [https://doi.org/10.1016/0006-8993\(90\)90227-3](https://doi.org/10.1016/0006-8993(90)90227-3)
- [68] Shi J, Barakat M, Chen D and Chen L 2018 Bicellular tight junctions and wound healing *Int. J. Mol. Sci.* **19** E3862
- [69] Novikova L N, Pettersson J, Brohlin M, Wiberg M and Novikov L N 2008 Biodegradable poly-beta-hydroxybutyrate scaffold seeded with Schwann cells to promote spinal cord repair *Biomaterials* **29** 1198–206
- [70] Yao Z A, Chen F J, Cui H L, Lin T, Guo N and Wu H G 2018 Efficacy of chitosan and sodium alginate scaffolds for repair of spinal cord injury in rats *Neural Regen. Res.* **13** 502–9
- [71] Herrmann J E *et al* 2008 STAT3 is a critical regulator of astrogliosis and scar formation after spinal cord injury *J. Neurosci.* **28** 7231–43
- [72] Hakim J S *et al* 2015 Positively charged oligo[poly(ethylene glycol) fumarate] scaffold implantation results in a permissive

- lesion environment after spinal cord injury in rat *Tissue Eng. A* **21** 2099–114
- [73] Hellal F *et al* 2011 Microtubule stabilization reduces scarring and causes axon regeneration after spinal cord injury *Science* **331** 928–31
- [74] Ruschel J *et al* 2015 Axonal regeneration. Systemic administration of ephothilone B promotes axon regeneration after spinal cord injury *Science* **348** 347–52
- [75] Dragunow M 2013 Meningeal and choroid plexus cells—novel drug targets for CNS disorders *Brain Res.* **1501** 32–55
- [76] Goritz C, Dias D O, Tomilin N, Barbacid M, Shupliakov O and Frisen J 2011 A pericyte origin of spinal cord scar tissue *Science* **333** 238–42
- [77] Soderblom C *et al* 2013 Perivascular fibroblasts form the fibrotic scar after contusive spinal cord injury *J. Neurosci.* **33** 13882–7